Corrugation in the Weakly Interacting Hexagonal-BN/Cu(111) System: Structure Determination by Combining Non-contact Atomic Force Microscopy and X-ray Standing Waves

Martin Schwarz[1], Alexander Riss[1]*, Manuela Garnica[1], Jacob Ducke[1], Peter S. Deimel[1], David A. Duncan[2]*, Pardeep Kumar Thakur[2], Tien-Lin Lee[2], Ari Paavo Seitsonen[3], Johannes V. Barth[1], Francesco Allegretti[1], Willi Auwärter[1]*

[1]*Technical University of Munich, Department of Physics, 85748 Garching, Germany.*

[2]*Diamond Light Source, Harwell Science and Innovation Campus, Didcot, OX11 0DE, United Kingdom.*

[3]*Département de Chimie, École Normale Supérieure, 24 rue Lhomond, F-75005 Paris, France.*

Corresponding Authors

* Willi Auwärter, Email: wau@tum.de

* Alexander Riss, Email: a.riss@tum.de

* David Duncan, Email: david.duncan@diamond.ac.uk

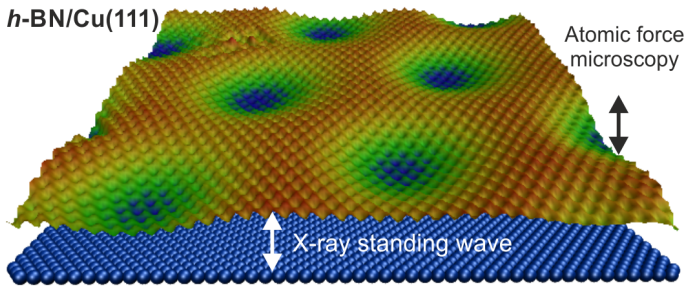

TOC figure

Abstract

Atomically thin hexagonal boron nitride (*h*-BN) layers on metallic supports represent a promising platform for the selective adsorption of atoms, clusters, and molecular nanostructures. Specifically, scanning tunneling microscopy (STM) studies revealed an electronic corrugation of *h*-BN/Cu(111), guiding the self-assembly of molecules and their energy level alignment. A detailed characterization of the *h*-BN/Cu(111) interface including the spacing between the *h*-BN sheet and its support - elusive to STM measurements - is crucial to rationalize the interfacial interactions within these systems. To this end, we employ complementary techniques including high-resolution non-contact atomic force microscopy (nc-AFM), STM, low-energy electron diffraction (LEED), X-ray photoelectron spectroscopy (XPS), the X-ray standing wave method (XSW), and density functional theory (DFT). Our multi-method study yields a comprehensive, quantitative structure determination including the adsorption height and the corrugation of the sp^2 bonded *h*-BN layer on Cu(111). Based on the atomic contrast in AFM measurements, we derive a measurable – hitherto unrecognized – geometric corrugation of the *h*-BN monolayer. This experimental approach allows to spatially resolve minute height variations in low-dimensional nanostructures, thus providing a benchmark for theoretical modeling. Regarding potential applications, *e.g.,* as template or catalytically active support, the recognition of *h*-BN on Cu(111) as a weakly bonded and moderately corrugated overlayer is highly relevant.

Keywords: hexagonal boron nitride, Cu(111), X-ray standing wave (XSW), atomic force microscopy (AFM), adsorption height, corrugation.

Two-dimensional hexagonal boron nitride (*h*-BN) grown on various transition metal substrates has attracted tremendous interest in the scientific community due to its fascinating properties like, *e.g.* inertness, high mechanical strength and an electronic bandgap, which are complementary to those of graphene and other two-dimensional materials.[1–3] Especially the structural similarity of *h*-BN monolayers to graphene, reflected in a small lattice mismatch of 1.6 %,[4] makes these materials compatible for applications in vertically stacked van-der-Waals heterostructures and in hybridized atomically flat layers.[5–9] Moreover, single-layer *h*-BN has shown its potential as a template to steer the adsorption of atoms, molecules and nanostructures with control of their spin and energy level alignment.[10–16] In addition, it has been demonstrated that metal-supported *h*-BN layers might serve as catalysts for oxygen reduction reactions.[17–20]

Depending on the interaction with the metal substrate, one can categorize the *h*-BN layer adhesion as strong [such as on the Rh(111), Ni(111) and Ir(111) surfaces] or weak [on the Pt(111), Cu(111) and Ag(111) surfaces].[21–27] The strength of the interaction, together with the lattice mismatch between *h*-BN and support determines the corrugation of the system, which forms a nanomesh in case of *h*-BN/Rh(111) and a flat overlayer with a minute height difference between boron and nitrogen in case of *h*-BN/Ni(111).[21,27,28] Cu(111) is a particularly interesting substrate as it features both a small lattice mismatch and a weak interaction with *h*-BN. Furthermore, the use of Cu foils as a support can be an economic route to large-scale *h*-BN synthesis *via* chemical vapor deposition (CVD).[3,23,29]

However, to realize the myriad of applications for this layer, and to integrate it into real devices *via* the bottom-up approach, a proper knowledge of the precise structure

of the *h*-BN is crucial. Density functional theory (DFT) calculations have, to date, struggled to describe the experimentally realized *h*-BN/Cu system in detail. Specifically the adsorption height of the *h*-BN layer, the key structural parameter in such a layered system, has been predicted to take a gamut of values, from 2.65 to 3.34 Å.[17,19,30–33] Therefore, determining this parameter experimentally to serve as an unambiguous benchmark is a necessary step towards predictive-level DFT calculations in this field.

Previous quantitative studies of the geometric structures of *h*-BN/Ir(111) and *h*-BN/Ni(111) have been pursued by X-ray standing waves (XSW) and X-ray photoelectron diffraction (PhD), respectively.[24,28] In case of the former system, a significant modulation of the *h*-BN layer was observed and modeled by two distinct *h*-BN species located at 2.20 ± 0.02 and 3.72 ± 0.02 Å, respectively, above the surface, a marked difference in adsorption height of ~ 1.5 Å.[24] The latter study, addressing *h*-BN/Ni(111), instead reported a uniform adsorption height of the entire *h*-BN layer above the outermost layer of Ni atoms of 2.11 ± 0.02 Å, *i.e.*, 0.1 Å closer to the substrate than even the lower adsorption height of the *h*-BN on Ir.[28] Although the corrugation of the *h*-BN/Ni(111) was a fitting parameter, no values were quoted. Now, by contrast to Ni(111) and Ir(111), Cu(111) is a comparatively noble substrate and, although a strong moiré pattern has been observed by STM, it was concluded that this reflects purely electronic modulations.[23,34]

While the lateral structure of two-dimensional layers is usually analyzed by means of scanning tunneling microscopy (STM), atomic force microscopy (AFM), standard low-energy electron diffraction (LEED) and PhD, a determination of the adsorption height, as well as the corrugation of two dimensional layers is notoriously difficult to obtain, even by high-resolution non-contact AFM (nc-AFM). Only elaborate LEED-I(V) and

surface X-ray diffraction studies gave access to these parameters, *e.g.,* for graphene on Ru(0001).[35,36] In the following, we present an in-depth structure determination of the *h*-BN/Cu(111) system with the lateral structure analyzed by means of STM and LEED and the vertical structure *via* a combination of nc-AFM, XPS, and XSW. The interpretation of the data is assisted by first-principle calculations. Ultimately, we introduce an approach to extract the detailed nature of an exemplary 2D sheet system *via* nc-AFM, which can also be applied to quantify the corrugation of other two-dimensional materials.

Results and Discussion

Lateral Structure of *h*-BN/Cu(111)

The lateral structure of *h*-BN/Cu(111) is investigated by means of STM and LEED. Here, we highlight our present findings on the basis of the results presented in our earlier studies,[23] which are consistent with reports from other groups.[37,38] Figure 1a displays the STM topography image of an extended *h*-BN domain on Cu(111) at 4 V bias voltage, where the electronic corrugation is visualized as a moiré superstructure.[23] In our previous studies the high symmetry registries, giving rise to different regions of the moiré, were labeled “hills” (corresponding to a $N_{top}B_{fcc}$ registry) and “valleys” (corresponding to a $N_{fcc}B_{hcp}$ registry). Following the notation of studies on *h*-BN/Rh(111) and *h*-BN/Ir(111)[21,24] the respective regions will be labeled pore (P) and wire (W) in this study (see Figure 2a) as justified by the observed geometric corrugation discussed below. The most abundant moiré periodicities observed are in the range from 4 to 15 nm and originate from different rotation angles of the *h*-BN lattice with respect to the copper substrate. All rotational domains were originally understood by a small spread (< 3°) in the angle between a slightly

stretched *h*-BN lattice and the Cu(111) substrate lattice and show the same electronic behavior in terms of their templating effect.[10,23]

The corresponding LEED pattern of a single layer of *h*-BN/Cu(111) is displayed in Figure 1b. The first-order Cu(111) substrate spots are surrounded by one concentric ring-like structure with a slightly larger k vector,[37,39] indicative of various rotational *h*-BN domains.[40] Maximum intensity of the *h*-BN ring is found in directions varying up to ± 4° from the main crystallographic directions of the copper substrate (Inset of Figure 1b). Local maxima are also observed at rotation angles of 30 ± 4° with respect to the close-packed directions of the substrate. Atomically resolved *h*-BN lattices observed in STM (Figure 1c and d) corroborate this finding. Analysis of the lattice parameters obtained from LEED measurements conducted at room temperature yields a lattice mismatch of 1.5 ± 0.1 %, slightly reduced compared to the 1.9 % mismatch reported by Roth *et al.*[37] and the nominal 2.0 % lattice mismatch between an isolated *h*-BN layer and the Cu(111) plane.[4,41] To accurately model experimentally observed moiré superstructures in graphene on metal systems, the consideration of multiple beatings per moiré unit cell appeared essential.[42,43] Indeed, such a modeling approach applied to *h*-BN/Cu(111) reveals the existence of large moiré periodicities even for *h*-BN domains rotated up to 30° (see Figure S1).

Scanning tunneling spectroscopy (STS) measurements probing the field emission resonances reveal a local work function difference of ~250 mV between high-symmetry positions within the moiré supercell (see Figure S2). Regions of bright contrast at a sample bias of 4 V in STM (pores) possess a lower local work function compared to the darker regions (wires), in agreement with our refined DFT calculations. A work function difference of 340 – 390 meV is calculated for high-symmetry registries of *h*-BN/Cu(111) with the Quantum ESPRESSO[44] code including

vdW-DF2-rB86[45,46] and vdW-DF-optB86[47] exchange-correlation functionals (see Supporting Information, Table 1). The discrepancy to our previously reported values[23] highlights the sensitive role of the exchange-correlation functional for a precise description of *h*-BN on metal systems. The local contact potential difference (CPD) obtained from Kelvin probe measurements (see Figure S3b) also confirms a lower work function at the pores but yields a clearly reduced work function modulation of 20 – 30 meV, presumably due to a considerable averaging over a larger area as compared to STS measurements.

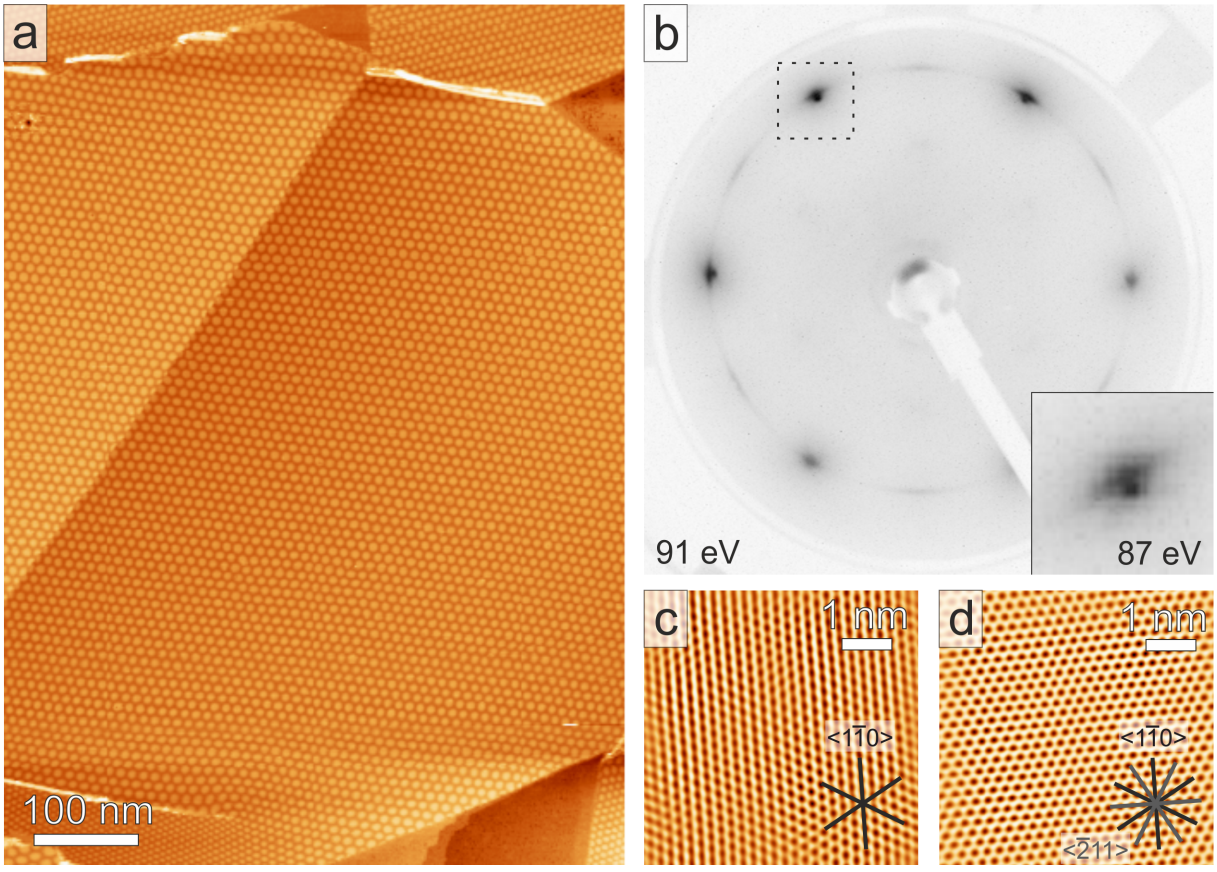

Figure 1 – Single layer of *h*-BN on Cu(111). **(a)** Large scale STM topography image showing extended and regular *h*-BN islands with domain sizes up to micrometer. Scan parameters: U_b = 4.0 V, I_t = 0.4 nA **(b)** Contrast inverted LEED pattern of a single layer *h*-BN/Cu(111) recorded at room temperature with an electron energy E = 91 eV. The Cu spots are surrounded by a ring originating from the *h*-BN lattice with highest intensity at a small azimuthal rotation relative to the (111) directions. At rotation angles of 30 ± 4° local intensity maxima are observed. Inset (recorded with E = 87 eV)

shows a zoom into the 1st order spot indicated by the dotted square. **(c)** and **(d)** show atomically resolved STM images of *h*-BN lattices (FFT-filtered). Black lines indicate the high-symmetry copper directions. The *h*-BN lattice in (c) is aligned along the Cu(111) directions, while in (d) it is rotated by almost 30° with respect to the copper. Scan parameters: (c) U_b = 0.11 V, I_t = 2.5 nA, (d) U_b = 0.23 V, I_t = 0.8 nA.

Vertical Structure of *h*-BN/Cu(111)

The mean adsorption height (see below) as well as the local corrugation of *h*-BN/Cu(111) are quantified by a combined nc-AFM and XSW interpretation. The XSW method has been widely applied to structural studies of surface adsorbates, to accurately determine the mean adsorption height. Quantifying the corrugation amplitude of the *h*-BN layer is, however, much less straightforward. Although XSW accurately measures with high precision the spatially averaged distribution center of the overlayer, the extracted distribution width from a single Bragg reflection can be strongly model-dependent. Laterally resolved measurements by nc-AFM are possible, however, the interaction forces between tip and sample can still be different, even for chemically equivalent species when different areas of the moiré super lattice are probed. Most notably, the different electronic structure across the moiré unit cell (see local work function measurements in Figure S2) is expected to lead to different electrostatic interactions.[34] Recent studies have estimated the molecular adsorption geometries utilizing force-distance maps obtained from nc-AFM.[48–50] Importantly, also the force-distance relationship can be significantly altered by the variation of electrostatic forces across the moiré supercell, thus making the applicability of this method more challenging.[51,52]

Corrugation – AFM measurements

To estimate the influence of electrostatic forces, bias-dependent nc-AFM measurements were carried out (see Figure S3). We have performed constant frequency shift (Δf) measurements with sample biases both, smaller (U_b = -0.1 V) and larger (U_b = 0.2 V) than the measured contact potential difference $U_b^* \approx 0.13$ - 0.16 V (see Figures S3b and c). The absence of contrast inversion in these measurements suggest that the observed corrugation of the *h*-BN in the nc-AFM measurements is not purely based on work function differences for the high-symmetry registries of the moiré unit cell. However, as the tip-sample distance is rather large in these measurements, which is necessary to maintain stable imaging conditions,[53] spatial averaging can play an important role and thus impedes a quantitative determination of the corrugation.

We recorded atomically resolved constant-height AFM images (Figure 2a and S7), where pore and wire regions are clearly discernible. Interestingly, this contrast can be inverted depending on the tip termination. In some cases the pores are imaged darker, *i.e.* more attractive than the wires (Figure 2a), in other cases this contrast is inverted (Figure S7). Such an inversion of contrast can originate from different work functions of the tip, which give rise to different electrostatic interactions with the sample. Strikingly, independent of the moiré contrast, the images show that the atomic contrast is significantly higher on the wire regions compared to the pore regions in the constant height images. This finding suggests a difference between the tip-sample distances of the wire and pore regions.

To quantify the corrugation of the *h*-BN layer we employed a method in which we calibrate the variation of the atomic contrast as a function of the tip height z (see Methods section). We define the atomic contrast by the Δf difference between the

darkest and the brightest regions at the length scale of a *h*-BN unit cell, expressed as Δf amplitude $A_{\Delta f}(z)$. Figure 2b and e show $A_{\Delta f}$ derived from constant-height scans for a series of tip heights on wire and pore regions. Selected slices are shown in Figure 2f,g (pore) and Figure 2h,i (wire) as well as in Figure S4. The obtained calibrations, $A_{\Delta f,W}$ and $A_{\Delta f,P}$, appear linear over a range of about 1 Å for both, wire and pore regions exhibiting similar slopes.

An averaged calibration curve (solid line in Figure 2b and e) correlates the Δf amplitude $A_{\Delta f}$ to a tip-sample distance $\Delta d_{tip\text{-}sample}$, *i.e.* $A_{\Delta f} \propto \Delta d_{tip\text{-}sample}$, allowing us to convert the atomic contrast in the large-scale constant-height image (Figure 2a) into a relative height map, $z_{calc}(A_{\Delta f})$, representing the geometric corrugation shown in Figure 2c. A clear corrugation is observed, closely resembling the *h*-BN moiré pattern, where the pores are lower than the wire regions. A height distribution histogram of the marked moiré unit cell is plotted in Figure 2d and reveals a total width of 0.64 Å. In analogy to the $\mu \pm 2\,\sigma$ ($\pm 1\,\sigma$) intervals used for Gaussian distributions, we calculated the height range encompassing 95% (68%) of the values to be 0.50 Å (0.26 Å). A sinusoidal fit to representative height profiles yields a peak-to-peak amplitude of 0.40 Å (Figure S11). Our DFT calculations (see Supporting Information, Table 1) indicate a height difference of 0.24 – 0.27 Å between high-symmetry sites of the *h*-BN unit cell, which show the same trend as our experimental results but underestimate the magnitude.

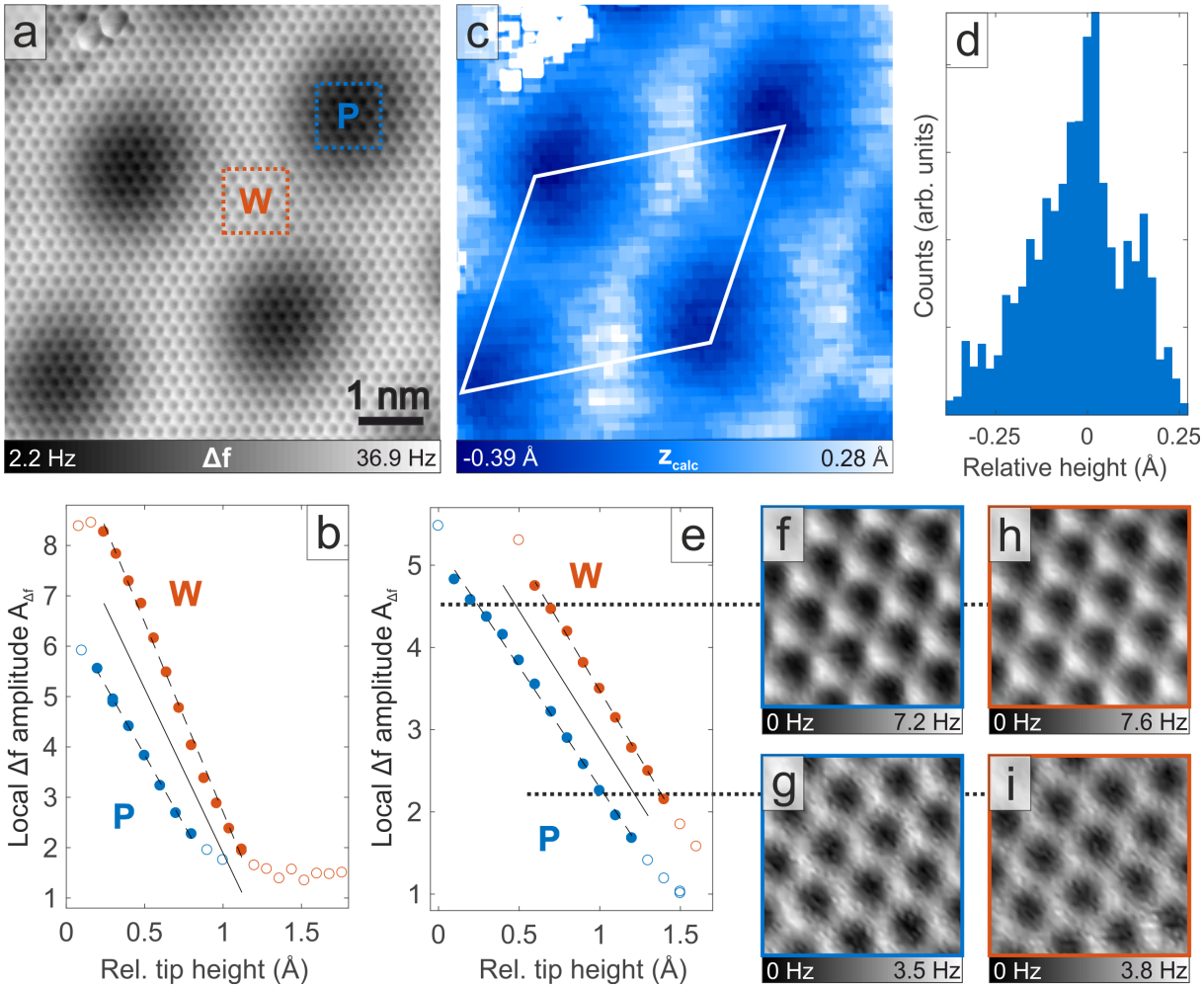

Figure 2 – Geometric corrugation of *h*-BN/Cu(111) determined from nc-AFM. **(a)** Constant-height AFM image of a single layer *h*-BN/Cu(111) showing the *h*-BN lattice together with the moiré unit cell. Orange (blue) square indicates the wire (pore) region of the moiré pattern. **(b)** Calibration curve $A_{\Delta f}(z)$ (solid line), obtained from the atomic *h*-BN contrast in pore (P) and wire (W) regions. Dashed lines represent linear fits of filled data points. The relative tip height is defined with respect to a reference point, which corresponds to the lowest tip height that was probed within the experiment. **(c)** Calculated height map $z_{calc}(A_{\Delta f})$ obtained by converting the atomic contrast in (a) into relative heights *via* the calibration shown in (b). The color scale represents the values within the unit cell, which is marked by a white rhombus. **(d)** Height distribution histogram for the indicated moiré unit cell. **(e)** Calibration curve $A_{\Delta f}$ (solid line) for a second measurement that is displayed in the Supporting Information, Figure S5, conducted with a different tip apex on a different sample spot. Again a similar characteristics is seen for pore and wire regions. **(f)-(i)** AFM scans associated with two different $A_{\Delta f}$ values, marked by dotted lines in (e), showing the atomic contrast of the *h*-BN lattice on pore [(f) and (g)] and wire regions [(h) and (i)]. Scan areas in (f)-(i) are 1×1 nm^2 and the color scale is Δf^{rel}. All images were acquired with 0 V bias and at 5 K.

Mean adsorption height: XPS and XSW

High-resolution soft X-ray core level spectra of *h*-BN/Cu(111) are displayed in Figure 3. Both B 1s and N 1s spectra are asymmetric with a characteristic shoulder at high binding energies.[34,54–56] This shoulder results from a clearly separate chemical species, and cannot be explained as a loss feature, as a distinct absorption profile was observed in the XSW measurements described below, which indicates significantly different adsorption heights for the two species. Therefore, we model the B 1s and N 1s spectra with two distinct components [B_0 (N_0) and B_{def} (N_{def}), see Methods section for details], whose parameters are summarized in Table 1. The primary B 1s / N 1s species (B_0/N_0, respectively) is assigned to the *h*-BN layer and the B 1s / N 1s shoulder (B_{def}/N_{def}, respectively) is assigned to defective, polymeric components[57] where the local B:N stoichiometry is no longer 1:1. This assignment is justified in the discussion. The binding energy difference between B_0 (N_0) and B_{def} (N_{def}) was found to be 0.6 eV (0.5 eV) (respectively).

Table 1 – Soft XPS parameters [a]

	E_b^0 (eV)	Γ (eV)	σ (eV)
B_0	190.4	0.08	0.52
B_{def}	191.0	0.08	0.42
N_0	398.0	0.11	0.46
N_{def}	398.5	0.11	0.40

[a] Peak position E_b^0, Lorentzian width Γ and Gaussian width σ obtained from the fits for the indicated components. Voigt lineshapes are used for the curve-fitting of the B 1s and N 1s core level spectra.

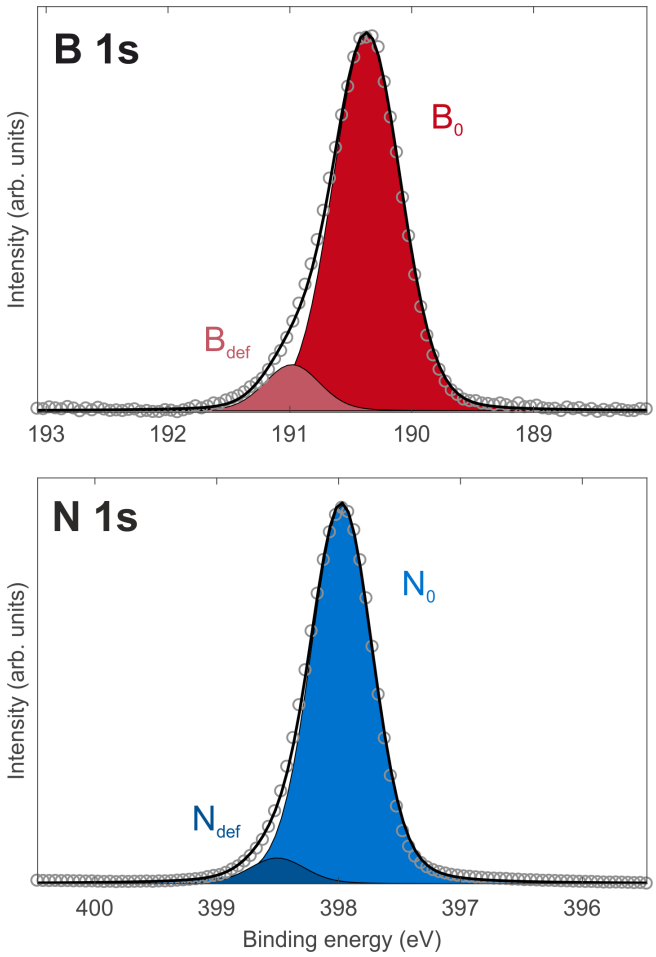

Figure 3 - High-resolution soft XPS N 1s and B 1s spectra for a single layer of *h*-BN/Cu(111). A Shirley background was subtracted from the data. The colored areas are fits of the indicated components. Solid black line is the sum of the fits. Photon energy of 641 eV was used for all spectra.

The mean adsorption height of *h*-BN on Cu(111) is obtained unambiguously through XSW analysis; the XSW method exploits the standing wave field that results from the interference between the incident and the diffracted X-ray beams under the Bragg condition for a substrate reflection H.[58] As the photon energy of the incident X-rays is scanned through the reflection, the standing wave field traverses half the Bragg plane spacing (d_H), leading to modulated absorption profiles (and thus photoelectron yields) of different chemical species, each with a distinct photon energy dependence that depends on the spatial distribution of the species. Such absorption profiles can be described by the dynamical diffraction theory of X-rays[59] with two fitting

parameters: the coherent position (p^H) and the coherent fraction (f^H). In simplistic terms, the former can be interpreted as the average position of a chemical species relative to the extended bulk Bragg planes in units of d_H and the latter is related to the distribution of these positions, through disorder (*e.g.* amorphous regions), a static variation (*e.g.* multiple adsorption sites), or a dynamic one (*e.g.* thermal vibrations). In particular, f^H can only take values between 0 and 1, and has contributions from the ordered fraction (C), a geometric factor (a_H) and the Debye-Waller factor (D_H) such that:

$$f^H = C \cdot a_H \cdot D_H, \quad (1)$$

which model, respectively, the level of order, the static geometric distribution, and the dynamic geometric distribution. For adsorbates with low atomic numbers, the Debye-Waller factor alone is typically around 0.9 at room temperature.

The result of our Cu(111) XSW analysis, utilizing the B 1s and N 1s core levels, is displayed in Figure 4 for B_0, B_{def}, N_0, and N_{def}. The absorption profiles of N_0 and B_0 show pronounced standing wave modulations with nearly identical shapes, indicating that the mean height is the same for both species; N_{def} and B_{def} exhibit a small but noticeable shift of their maxima and minima, with respect to N_0 and B_0, towards a higher photon energy and a slight reduction of the modulation amplitudes, indicating a lower adsorption height and a greater spread in positions for these minority species. The coherent positions and fractions deduced from the XSW analysis for all four chemical species are summarized in Table 2.

Assuming a bulk terminated Cu(111) surface the average adsorption height, $\overline{h}$, is related to p^{111} as $\overline{h} = (p^{111} + n)d_{111}$, where the integer n accounts for the periodic nature of the standing wave field. As the d_{111} spacing for Cu(111) is 2.087 Å[60] and with the measured values for p^{111} (shown in Table 2), it can be easily verified that

only n = 1 renders physically reasonable values for $\bar{h}$. Thus, the average adsorption heights are determined to be $\bar{h}_0$ = 3.37 ± 0.04 Å (3.39 ± 0.04 Å) for the main component N_0 (B_0) and $\bar{h}_{def}$ = 3.30 ± 0.06 Å (3.26 ± 0.09 Å) for the defective component N_{def} (B_{def}). Furthermore, our analysis reveals a f^{111} of 0.71 ± 0.02 (0.65 ± 0.03) for N_0 (B_0), which is significantly lower than the value expected for a perfectly flat *h*-BN layer ($f^H \geq 0.9$), and a further reduced f^{111} of 0.34 ± 0.07 (0.40 ± 0.03) for N_{def} (B_{def}).

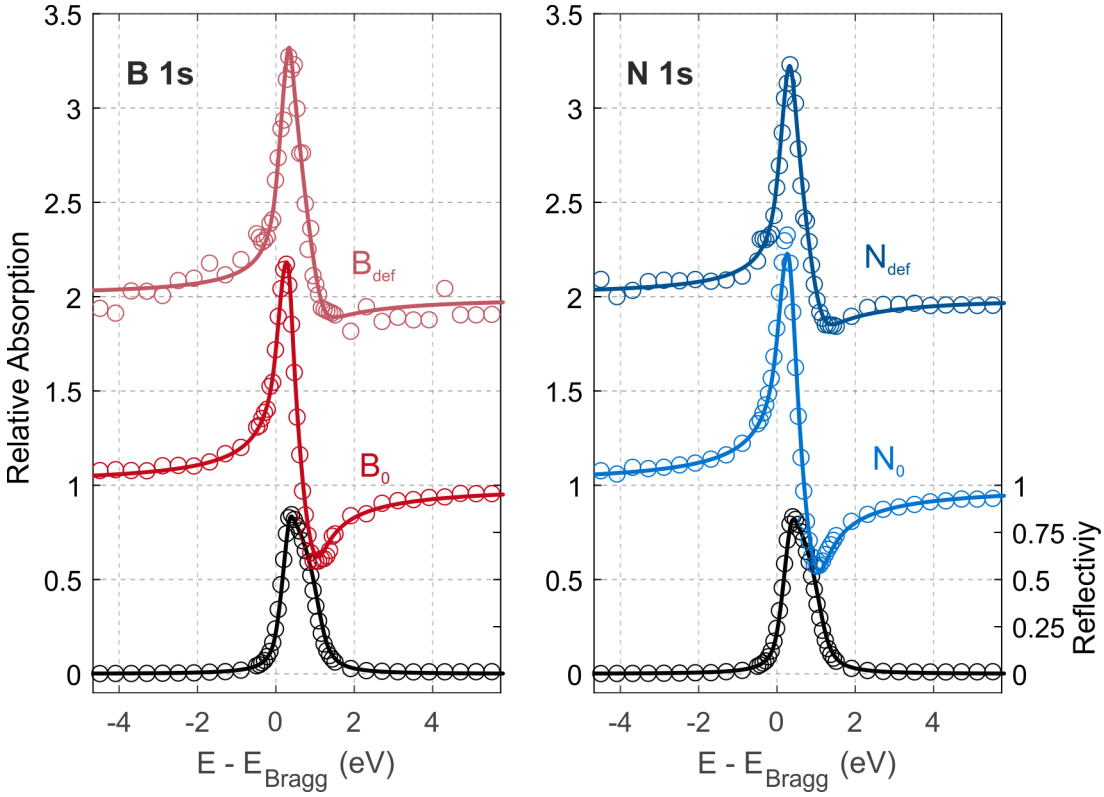

Figure 4 - X-ray standing wave absorption profiles of B 1s (red) and N 1s (blue) for a single layer of *h*-BN/Cu(111). Solid lines are fits to the data. Black data points correspond to the Cu(111) reflectivity curve. The XSW profiles of the defective *h*-BN components B_{def} and N_{def} are offset vertically +1 for clarity.

Table 2 – Structural parameters obtained from XSW measurements [a]

	Main components			Defective components		
	p^{111}	Adsorption height $\overline{h}_0$ (Å)	f^{111}	p^{111}	Adsorption height $\overline{h}_{def}$ (Å)	f^{111}
B 1s	0.63 ± 0.02	3.39 ± 0.04	0.65 ± 0.03	0.56 ± 0.04	3.26 ± 0.09	0.34 ± 0.07
N 1s	0.62 ± 0.02	3.37 ± 0.04	0.71 ± 0.02	0.58 ± 0.03	3.30 ± 0.06	0.40 ± 0.03

[a] Summary of the structural parameters obtained from the XSW measurement shown in Figure 4: coherent position p^{111}, the corresponding adsorption height of the *h*-BN layer on Cu(111), and coherent fraction f^{111} for both chemical species B/N_0 and B/N_{def}.

Discussion

The XPS binding energies of the main B 1s and N 1s components (B_0: 190.4 eV, N_0: 398.0 eV) are in very good agreement with previous studies of *h*-BN/Cu(111).[54] These values are characteristic for physisorbed systems, midway between the ones of *h*-BN/Au (189.8 eV and 397.6 eV) and the ones of *h*-BN/Ag(111) (190.8 eV and 398.3 eV).[40,61] The XP core-level spectra of B 1s and N 1s are asymmetric with a shoulder at high binding energies and both 1s levels are best described by two Voigt functions, rather than an asymmetrical line shape (*e.g.* Doniach-Šunjić). This assignment is in contrast to previous publications on the *h*-BN/Cu(111) system,[54] where an asymmetrical peak shape has also been observed but the peaks were modeled with a single component. In the *h*-BN/Ir(111) system[24] the asymmetrical lineshape was assigned to the presence of “strongly” and “weakly” bound regions of the *h*-BN layer. This was justified by the XSW measurements indicating that the minority component was adsorbed 1.5 Å closer to the substrate than the majority component. However, the difference in adsorption height of the two components in *h*-BN/Cu(111) is only ~0.1 Å (15 times smaller than on Ir), but yet the binding energy shifts observed, ~0.5 / 0.6 eV, are comparable in magnitude to those observed for

h-BN on Ir(111) (0.8 / 0.9 eV). It is highly improbable that such a large binding energy difference could originate from such a minor difference in adsorption height. In fact, the XPS binding energies of the N 1s and B 1s core-levels, in *h*-BN/Cu(111) and *h*-BN/Ir(111) are remarkably similar, despite the difference in substrate, interaction strength, corrugation and adsorption height. Finally, DFT calculations (see Supporting Information) reveal only a modest N 1s binding energy variation between the weakly bound wire regions and the more strongly bound pore regions, that is too small to explain the difference observed in our combined XPS-XSW analysis. Therefore, it is inferred that the two components are inherently chemically different, and do not arise from a geometric corrugation in the layer. Effects from wrinkles within the layer and from step edges, domain boundaries and edge terminations as possible origin are also excluded due to their low abundance. Potentially, there could be a chemical difference between the *h*-BN domains mostly aligned azimuthally along the $< 1\bar{1}0 >$ symmetry directions of the substrate surface and the domains mostly aligned along the $< \bar{2}11 >$ directions. It is clear from the recorded LEED pattern (Figure 1b) that the *h*-BN layers that align mostly along the $< \bar{2}11 >$ results in smaller or fewer islands, however there is no indication, from the STM images (Figures 1c and 1d), of the $< \bar{2}11 >$ aligned islands being rougher than the $< 1\bar{1}0 >$ aligned islands, as the lower coherent fraction observed for N_{def}/B_{def} would suggest. Further, our DFT calculations suggest that no significant change in the mean adsorption height of the rotated *h*-BN domains would be expected.

The significant difference between B_0:B_{def} and N_0:N_{def} ratios (10:1 and 16:1, respectively) would further rule out the possibility that the minor components represent a different crystalline *h*-BN layer. Occasionally, in the STM images, inhomogeneous *h*-BN moiré patches (see Figure S7d) formed by strain, were

observed, which could potentially result in chemically different atomic species.[62] They were, however, not observed frequently enough to solely account for the observed B_0:B_{def} and N_0:N_{def} ratios. Instead, the more likely origin of these components are molecular polymeric fragments,[57] constrained inside triangular shaped holes that are found across the entire substrate (Figure 1a and Figure S7c). As atomic nitrogen desorbs from Cu(111) at around 750 K,[63] whereas atomic B melts into the Cu(111) substrate (Ref. [54] and Figure S8), a stoichiometric B:N deficiency in these fragments might exist, however, this deficiency results in a lowered binding energy for boron.[54] Conversely, assuming these polymeric fragments to be stoichiometrically abundant, presumably leading to the formation of sp^3 bonds, a significant shift towards a higher binding energy can be rationalized.[57] In agreement with recently published calculations on defective *h*-BN nanosheets,[64] we find that the defective components are closer to the copper substrate. Finally, as there is likely a continuum of such polymeric fragments (*e.g.* polyaminoborane, polyiminoborane, polyaminoborazine *etc.*), as can be observed in the mixture of species present in the triangular shaped holes in the STM images, the origin of the dramatically lower coherent fractions also becomes clear.

Based on these considerations, we focus on the majority *h*-BN species on Cu(111) and we show that combined AFM and XSW measurements yield a consistent picture regarding the geometric structure of the *h*-BN layer. Our AFM analysis displays measureable differences in the adsorption heights of the wire and pore regions. Regarding the validity of the experimentally determined corrugation of the *h*-BN layer *via* AFM analysis of the atomic contrast, two questions need to be investigated: (i) how is the atomic contrast influenced by tip-sample interactions that can be different for the wire and pore regions, and (ii) what is the influence of the AFM tip on the *h*-BN layer? To shed light on the first question, let us consider a hypothetical

layer that exhibits a geometric corrugation and is composed of entities that show exactly the same tip-sample interaction across the whole layer. Here, the measurement of the Δf amplitude *versus* tip height would yield calibration curves that exhibit exactly the same z-dependence, but are offset along the z-axis, reflecting the geometric corrugation. This is the behavior that is observed in our experiments. In particular, it can be seen that the z-dependence of the local Δf amplitude is almost the same for the respective wire and pore regions in the two measurement series shown in Figure 2. These series were performed on different areas of the surface with different tip configurations. Thus, the calibration curves may vary from experiment to experiment, but, importantly the wire and pore regions exhibit similar characteristics. However, we want to point out that, particularly in the experiment corresponding to the data shown in Figures 2a-d, small differences *can* be seen in the z-dependence of the local Δf amplitude for wire and pore. Apart from a slight difference in the slope of the calibration curves, the deviation from the near-linear regime at close tip sample-distances sets in earlier on the pore areas, *i.e.* at lower local Δf amplitudes (Figure 2b). These differences are much less pronounced in the second measurement series (Figures 2e-i). Here, the z-dependence of the local Δf amplitude is almost identical for wire and pore areas. The height distributions derived from both measurement series are comparable, suggesting that the slight differences between the wire and pore regions do not substantially affect the results. Further evidence supporting that the local Δf amplitude is a useful measure for the tip-sample distance comes from the atomic features in the calibration scans: AFM scans corresponding to local Δf amplitudes of $A_{\Delta f} \approx 6$Hz (Figures 2f, h) and $A_{\Delta f} \approx 3$Hz (Figures 2g, i) are shown for both wire and pore regions. Note, that in order to obtain the same $A_{\Delta f}$ for the respective regions, the tip height has to be lowered by ~ 0.4 Å on the pore regions. The images in Figures 2g and i ($A_{\Delta f} \approx 3$Hz) show a hexagonal

lattice with a honeycomb-like appearance, which develops into a rather triangular appearance at higher $A_{\Delta f}$ in Figures 2f and h ($A_{\Delta f} \approx 6$Hz). The measurements reveal that the Δf amplitude is correlated with the (asymmetric) features in the atomic contrast, which can be assumed to reflect the tip-sample distance.

To estimate the influence of the tip on the measurements, we analyzed the dissipation in the AFM experiments. Upon decrease of the tip-sample distance, the dissipation increases by up to 10% in the linear regime in the calibration curves. For the closest tip-sample distances the dissipation channel shows a pronounced contrast that correlates with the *h*-BN lattice (see Figure S6). A noticeable change in dissipation hints at the tip exhibiting an influence on the *h*-BN layer, presumably a geometric distortion as discussed in literature.[65–71] However, the similarity of the z-dependence of the local Δf amplitude, as well as of the atomic features in the AFM images, suggest that the influence of the tip on wire and pore regions is comparable. Based on these considerations, it is justified to assume that in our experiments, the local Δf amplitude can be directly correlated with relative height differences.

The XSW measurement yields an average adsorption height of the *h*-BN layer of $\overline{h}_0 = 3.38 \pm 0.06$ Å with boron and nitrogen sitting effectively at the same height as expected for a weakly interacting, physisorbed two dimensional network. Within the uncertainties, the adsorption height is comparable to the bulk *h*-BN interlayer spacing (3.33 Å) at room temperature.[72] The coherent fractions of 0.71 for N 1s and 0.65 for B 1s suggest a variation in the adsorption height arising from a combination of the effects of an imperfect crystallinity of the *h*-BN layer and the geometric corrugation of the crystalline *h*-BN layer in addition to thermal vibrations of the B and N atoms. Vibrational amplitudes can be estimated using the Debye temperature of Cu (~320 K at room temperature)[73] and bulk *h*-BN (~410 K at room temperature),[72] which results

in a root mean square (rms) vibrational amplitude of ~ 0.08 Å and ~ 0.15 Å, respectively. If these two vibrations are uncoupled, then the net rms vibrational amplitude of the *h*-BN layer will be ~ 0.17 Å. These values result in a Debye-Waller factor of 0.88 and thus, cannot be used to solely explain the significantly lower coherent fractions observed here. Indeed, in addition to this dynamic distribution of positions, in order to model a coherent fraction of ~ 0.7, a static distribution is also required. Based on the experimentally observed high quality of the sample, it is unlikely that the non-crystalline areas of the *h*-BN layer (*e.g.* at step edges on the Cu(111) surface, at domain boundaries between different rotations of the *h*-BN layer, *etc.*) are sufficient enough in size to result in an ordered fraction that differs significantly from 1. If the ordered fraction is effectively unity, and the Debye-Waller factor is 0.88, then, by equation (1), the geometric factor must be in the order of 0.8. As the various orientations of the *h*-BN layer are predicted (by DFT) to adsorb at effectively the same height, the most likely explanation for such a geometric factor is a corrugation in the *h*-BN layer. If either a Gaussian or an uniform height distribution is used to model such a geometric factor of the *h*-BN layer, then a corrugation with a 2σ of 0.45 Å or a total width of 0.75 Å, respectively, is required (see Figure S9). The height distribution, obtained *via* AFM measurements of the atomic contrast (Figure 2d), indicates a total width of 0.64 Å and a geometric factor of 0.92. Using this geometric factor, combined with the above Debye-Waller factor, a coherent fraction of 0.81 is obtained (compared to 0.71 ± 0.02 and 0.65 ± 0.03, for B and N atoms, respectively). The resulting profile, shown in Figure 5a (orange curve), is in remarkably good agreement with the experiment (blue curve), and the remaining difference can now likely be explained by the various effects discounted above: *e.g.* non-crystalline areas of the *h*-BN layer, step edges, *etc.* Therefore, we can conclude that the coherent fraction, extracted for the majority species of the *h*-BN on Cu(111),

results from a highly crystalline *h*-BN layer with a peak-to-peak geometric corrugation in the order of ~ 0.6 Å. To illustrate this corrugation and its scale, Figure 5b shows a 3D plot of the calculated height map $z_{calc}(A_{\Delta f})$ and Figure 5c a cross-section of the same height map in comparison to the adsorption height of the *h*-BN layer above the Cu(111) substrate. The geometric corrugation in the *h*-BN layer, which is already smaller than the atomic radii of either element, is spread over a length scale of nanometers, such that neighbouring atoms are effectively co-planar. Nevertheless, in this weakly interacting system, the corrugation amounts to a significant fraction, about 15-25%, of the mean adsorption height. Based on our DFT calculations in the (1x1) cell at different lateral registries, we expect the corrugation of the terminal Cu layer under the *h*-BN to be below 0.002 Å, *i.e.* the Cu substrate is considered to be planar (Figure 5c). Before concluding, we briefly discuss our findings in relation to our previous report on *h*-BN/Cu(111).[23] As the electronic interface state was observed in any region below the *h*-BN, we ruled out strong spatially localized *h*-BN –Cu interactions and thus a major geometric corrugation.[23] This interpretation is consistent with our present findings, where the *h*-BN – Cu separation exceeds 2.9 Å in any region (Figure 5c). Our previous DFT results yielded a corrugation of 0.16 Å and 0.04 Å for a moiré supercell and a 1x1 structure, respectively. We thus considered the *h*-BN overlayer to be topographically smooth.[23] In view of our present experiments and the refined DFT modeling, this assignment was not precise. Even though moderate corrugations with amplitudes much smaller than the nanometer-scale moiré periodicity in sp^2 layers are often considered negligible,[74] we now recognize – and emphasize – the non-planar nature of *h*-BN on Cu(111). At first sight, the combination of a large mean adsorption height reminiscent of the bulk *h*-BN layer separation with a relevant electronic and geometric modulation seems puzzling. However, we would like to point out that even single-crystal *h*-BN surfaces are not

imaged as perfectly planar by AFM[75] and considerable stacking-induced electronic modifications are described in bilayer *h*-BN or sp^2 heterostructures.[76,77] It is intriguing to envision *h*-BN morphologies in surface-supported sheets reminiscent of non-planar distortions anticipated for free-standing sp^2 sheets.

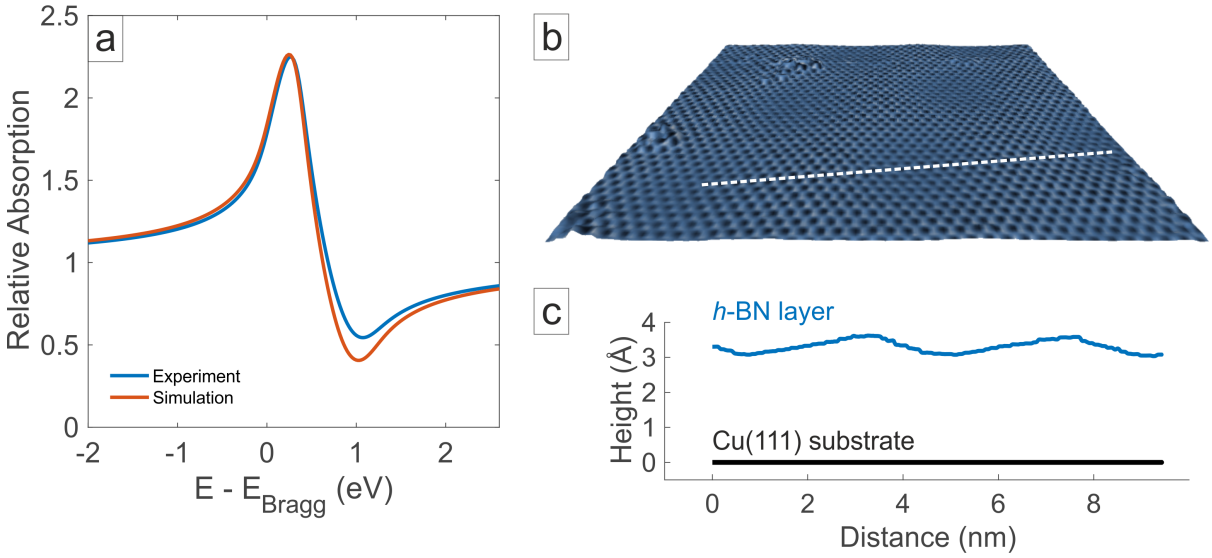

Figure 5 – **(a)** Comparison between the experimental (blue line) and a simulated (orange line) XSW absorption profile. For the simulation, the height distribution obtained from our AFM measurements was utilized. **(b)** 3D representation of the calculated height map z_{calc} overlayed with the corresponding high-pass filtered Δf image showing the corrugation of the *h*-BN layer on Cu(111) relative to its lateral dimension. Size: 10 × 10 nm^2. **(c)** Illustration of the *h*-BN/Cu(111) corrugation relative to its adsorption height. The *h*-BN layer is displayed as line profile extracted from the calculated height map z_{calc} as indicated in the 3D plot in (c) (white dashed line).

Conclusions

In conclusion, we presented a multi-method study that provides a complete, quantitative structure determination of the sp^2 bonded *h*-BN layer on Cu(111). The lateral structure is elucidated *via* complementary STM and LEED measurements giving insight into the azimuthal epitaxial relation of *h*-BN to Cu(111).

The mean absolute spacing between *h*-BN layer and copper substrate was found to be $\bar{h}_0$ = 3.38 ± 0.06 Å based on XSW measurements. We further introduce an

experimental method that allows the local *h*-BN corrugation to be determined *via* analysis of the atomic contrast in AFM measurements. The pore areas of the *h*-BN layer were observed to be 0.3 – 0.7 Å closer to the Cu(111) substrate, contrasting the hitherto assumed flat *h*-BN geometry. The obtained value for the local corrugation is in good agreement with the spatially averaged XSW results, providing insights in the physical origin of the coherent fraction.

This study further provides a clear benchmark for theoretical calculations in terms of the mean adsorption height as well as the corrugation of the layer. DFT calculations based on the latest exchange-correlation functionals can yield the values of the mean adsorption height and the corrugation with good agreement.

The described AFM technique – presumably even applicable to similar STM measurements – enables to determine relative height differences in two-dimensional layers, as well as in large polycyclic molecules. Its combination with XSW thus provides exciting opportunities for a detailed structure determination at the nanoscale.

Methods

Single layer *h*-BN was grown on Cu(111) in the UHV chamber of an LT-STM/AFM system at the Technical University of Munich and the preparation chamber of the I09 end station at Diamond Light Source (DLS) following the established procedure.[23] The base pressure in both systems was $<5\times10^{-10}$ mbar. The Cu(111) crystal was cleaned by repeated sputter and annealing cycles. In the UHV chamber in Munich the sample was held at 1080 K and positioned in close vicinity of a needle doser through which the borazine ($B_3N_3H_6$) was introduced, resulting in a chamber pressure

7×10^{-7} mbar for 5 min. At I09 the borazine was exposed to the sample (also held at 1080 K – monitored by pyrometer) by back filling of the chamber to 7×10^{-6} mbar for 25 minutes resulting in a total exposure of 7900 L. The higher pressure was to compensate for the lack of directional dosing at the I09 end station. The sample was then allowed to cool at a rate of 0.7 K/s. Both preparation conditions result in a single layer of *h*-BN and show the same characteristic LEED patterns. XP survey spectra showed no significant components other than B, N and Cu. STM/nc-AFM measurements were conducted at 5 K. All STM images were recorded in constant current mode using an electrochemically etched tungsten tip. Nc-AFM measurements were performed with a qPlus tuning fork sensor (resonance frequency ~30 kHz, oscillation amplitude 80 pm, Q value ~ 46000) operated in the frequency modulation mode.[78] The tip was prepared by indentation into bare Cu(111) and used without deliberate (CO-)functionalization.

The actual corrugation of the *h*-BN layer was obtained with an experimental method in which we correlate the atomic contrast observed in the AFM frequency shift Δf to a height difference. First, the local atomically resolved *h*-BN lattice was measured in a series of constant height scans with different tip heights (Figures 2f-i and Figure S4). Hereby, small-size images of 1×1 nm^2 were acquired on pore and wire regions. A Gaussian high-pass filter (σ of 0.15 nm) and a low-pass filter (σ of 0.05 nm) were applied for background correction and noise reduction, respectively. For each pixel in the small-size images, the Δf amplitude $A_{\Delta f}$ is determined as the difference between the brightest and darkest regions in a surrounding square box with side lengths of 0.28 nm, 10% bigger than the *h*-BN unit cell. By averaging over all pixels in each image, the average Δf amplitudes on wire ($A_{\Delta f,W}$) and pore regions ($A_{\Delta f,P}$) were determined and plotted as a function of the relative tip height (see Figures 2b and e). The tip height is defined with respect to a reference point that corresponds to the

lowest tip height that was probed within the experiment. No noticeable influence of piezo creep and thermal drift was found as verified by repeated calibration scans in both directions, *i.e.* increasing and decreasing relative tip heights. An averaged linear calibration curve $A_{\Delta f}$ (solid lines in Figures 2b and e) is obtained from the linear fits to $A_{\Delta f,W}$ and $A_{\Delta f,P}$. The local Δf amplitude $A_{\Delta f}$ is proportional to the tip-sample distance $\Delta d_{tip\text{-}sample}$, *i.e.* $A_{\Delta f} \propto \Delta d_{tip\text{-}sample}$. Utilizing this relationship, the large-area AFM constant-height image of the *h*-BN layer (Figure 2a) can be translated into a calculated height map $z_{calc}(A_{\Delta f})$ (Figure 2c) by converting the local Δf amplitude of each pixel of the constant-height image into a height difference.

The XPS and XSW experiments were carried out at the I09 end station of DLS. All high-resolution core-level spectra taken with soft X-rays were excited with a photon energy of 641 eV. For the X-ray standing wave measurements, the X-ray beam was defocused to approximately 400×400 μm^2 and was stepped over the sample such that each XSW curve was acquired at a different sample position to avoid potential beam damage to the *h*-BN layer and sample crystallinity. Possible beam damage was monitored by comparing the B 1s and N 1s XP spectra before and after each XSW measurement, where no changes were detected. The hemispherical electron analyzer, a VG Scienta EW4000 HAXPES, was mounted with an angle of 90° with respect to the incident synchrotron light and has an acceptance angle of ±28°. The XSW measurements were acquired at almost normal incidence to the reflection plane (specifically with a Bragg angle of ~+2.5°), and the intensity of the crystal Bragg reflection was measured simultaneously to the absorption profiles *via* a fluorescent screen mounted on the port of the incident X-ray beam by means of a CCD camera.

The XSW scans were acquired from the (111) Bragg reflection of Cu (E_{Bragg} ~ 2972 eV at 300 K). Prior to each XSW scan, a (111) Bragg reflection was

acquired and used to set the central photon energy for the XSW scan and then the subsequent scan was acquired over a photon energy window of 10 eV around the central photon energy. The measurements were repeated over 20 unique spots, resulting in 10 individual B 1s and N 1s XSW data sets, which were then averaged to improve the signal to noise ratio. The uncertainty of the given structural parameters reflects the spread of results obtained by analyzing each measurement individually. The B 1s and N 1s peaks were fitted with two Voigt profiles, each given by a convolution of independent Gaussian $G(E_b, \sigma)$ and Lorentzian $L(E_b, \Gamma)$ contributions:[79]

$$\text{Voigt}(A, E_b, E_b^0, \Gamma, \sigma) = A \cdot \delta(E_b - E_b^0) \times G(E_b, \sigma) \times L(E_b, \Gamma),$$

where A is the amplitude, E_b is the photoelectron binding energy scale, E_b^0 is the central binding energy of the Voigt profile, σ is the FWHM of the Gaussian, and Γ the HWHM (half-width at half-maximum) of the Lorentzian. The chosen widths of the Lorentzian components are in good agreement with reported core-hole lifetimes of B 1s and N 1s, respectively.[80] The Gaussian and Lorentzian lineshapes are both normalized, prior to convolution, to have an integrated area of 1. The Cu 3p peak, used to define the binding energy of the XP spectra, was fitted with a convolution of a Doniach-Šunjić function with a Gaussian lineshape (see Figure S10). The integrated intensities of B 1s and N 1s photoemission peaks were used to obtain the relative X-ray absorption of the B and N atoms, respectively. Non-dipolar effects in the angular dependence of the photoemission were accounted for with the asymmetry parameter Q which was calculated theoretically using the angle that corresponded to the average angle weighted by emission intensity at an off Bragg energy (θ = 18° where θ is as defined in Ref. [81]).

To simulate the effect of the various height distributions (either extracted from the nc-AFM measurement or given by a Gaussian/rectangular function) on the geometric factor, and thus the coherent fraction, the structural parameters f^{111} and p^{111} were expressed as the amplitude and phase (respectively) of a Fourier component of the adsorption site, projected along the (111) direction of the Cu crystal. This component can then be expressed by an integral, between $p^{111} = 0$ and $p^{111} = 1$, and an associated probability assigned to each position, as described in equation (1) in the supporting information and equation (17) of Ref [82]. The length of the vector represents the coherent fraction and the angle is defined by the coherent position. Each individual component within the respective distribution was assumed to have a coherent fraction of 0.88 (taking into account the vibrational amplitudes discussed above) and weighted by a factor dependent on the distribution. An exemplary profile is shown in Figure 5a together with its structural fit parameter. Simulated XSW absorption profiles for a Gaussian and a uniform height distribution are provided in the supporting information (Figure S9).

Acknowledgments

This work is supported by the European Research Council Consolidator Grant NanoSurfs (No. 615233) and the Munich-Center for Advanced Photonics (MAP). M.G. would like to acknowledge the H2020-MSCA-IF-2014 programme. W.A. acknowledges funding by the Deutsche Forschungsgemeinschaft *via* a Heisenberg

professorship. We thank Diamond Light Source for the award of beam time and funding. Further, we acknowledge Centro Svizzero di Calcolo Scientifico in Lugano, Switzerland for the computing time with project uzh11. We thank M. Sokolowski for fruitful discussions.

Competing financial interests

The authors declare no competing financial interests.

Supporting Information Available

Additional experimental STM, STS, AFM, DFT and XPS/XSW data. This material is available free of charge *via* the Internet at http://pubs.acs.org.

References

(1) Shi, Y.; Hamsen, C.; Jia, X.; Kim, K. K.; Reina, A.; Hofmann, M.; Hsu, A. L.; Zhang, K.; Li, H.; Juang, Z.-Y.; Dresselhaus, M. S.; Li, L.-J.; Kong, J. Synthesis of Few-Layer Hexagonal Boron Nitride Thin Film by Chemical Vapor Deposition. *Nano Lett.* **2010**, *10*, 4134–4139.

(2) Watanabe, K.; Taniguchi, T.; Kanda, H. Direct-Bandgap Properties and Evidence for Ultraviolet Lasing of Hexagonal Boron Nitride Single Crystal. *Nat. Mater.* **2004**, *3*, 404–409.

(3) Kim, K. K.; Hsu, A.; Jia, X.; Kim, S. M.; Shi, Y.; Hofmann, M.; Nezich, D.; Rodriguez-Nieva, J. F.; Dresselhaus, M.; Palacios, T.; Kong, J. Synthesis of Monolayer Hexagonal Boron Nitride on Cu Foil Using Chemical Vapor Deposition. *Nano Lett.* **2012**, *12*, 161–166.

(4) Paszkowicz, W.; Pelka, J. B.; Knapp, M.; Szyszko, T.; Podsiadlo, S. Lattice Parameters and Anisotropic Thermal Expansion of Hexagonal Boron Nitride in the 10-297.5 K Temperature Range. *Appl. Phys. A* **2002**, *75*, 431–435.

(5) Geim, A. K.; Grigorieva, I. V. Van der Waals Heterostructures. *Nature* **2013**, *499*, 419–425.

(6) Oshima, C.; Nagashima, A. Ultra-Thin Epitaxial Films of Graphite and Hexagonal Boron Nitride on Solid Surfaces. *J. Phys. Cond. Matter* **1997**, *9*, 1–20.

(7) Decker, R.; Wang, Y.; Brar, V. W.; Regan, W.; Tsai, H.-Z.; Wu, Q.; Gannett, W.; Zettl, A.; Crommie, M. F. Local Electronic Properties of Graphene on a BN Substrate *via* Scanning Tunneling Microscopy. *Nano Lett.* **2011**, *11*, 2291–2295.

(8) Hwang, B.; Hwang, J.; Yoon, J. K.; Lim, S.; Kim, S.; Lee, M.; Kwon, J. H.; Baek, H.; Sung, D.; Kim, G.; Hong, S.; Ihm, J.; Stroscio, J. A.; Kuk, Y. Energy Bandgap and Edge States in an Epitaxially Grown Graphene/h-BN Heterostructure. *Sci. Rep.* **2016**, *6*, 31160.

(9) Ci, L.; Song, L.; Jin, C.; Jariwala, D.; Wu, D.; Li, Y.; Srivastava, A.; Wang, Z. F.; Storr, K.; Balicas, L.; Liu, F.; Ajayan, P. M. Atomic Layers of Hybridized Boron Nitride and Graphene Domains. *Nat. Mater.* **2010**, *9*, 430–435.

(10) Joshi, S.; Bischoff, F.; Koitz, R.; Ecija, D.; Seufert, K.; Seitsonen, A. P.; Hutter, J.; Diller, K.; Urgel, J. I.; Sachdev, H.; Barth, J. V.; Auwärter, W. Control of Molecular

Organization and Energy Level Alignment by an Electronically Nanopatterned Boron Nitride Template. *ACS Nano* **2014**, *8*, 430–442.

(11) Kumar, A.; Banerjee, K.; Liljeroth, P. Molecular Assembly on Two-Dimensional Materials. *Nanotechnology* **2017**, *28*, 82001.

(12) Urgel, J. I.; Schwarz, M.; Garnica, M.; Stassen, D.; Bonifazi, D.; Ecija, D.; Barth, J. V.; Auwärter, W. Controlling Coordination Reactions and Assembly on a Cu(111) Supported Boron Nitride Monolayer. *J. Am. Chem. Soc.* **2015**, *137*, 2420–2423.

(13) Schulz, F.; Ijäs, M.; Drost, R.; Hämäläinen, S. K.; Harju, A.; Seitsonen, A. P.; Liljeroth, P. Many-Body Transitions in a Single Molecule Visualized by Scanning Tunnelling Microscopy. *Nat. Phys.* **2015**, *11*, 229–234.

(14) Jacobson, P.; Herden, T.; Muenks, M.; Laskin, G.; Brovko, O.; Stepanyuk, V.; Ternes, M.; Kern, K. Quantum Engineering of Spin and Anisotropy in Magnetic Molecular Junctions. *Nat. Commun.* **2015**, *6*, 8536.

(15) Jacobson, P.; Muenks, M.; Laskin, G.; Brovko, O.; Stepanyuk, V.; Ternes, M.; Kern, K. Potential Energy-Driven Spin Manipulation *via* a Controllable Hydrogen Ligand. *Sci. Adv.* **2017**, *3*, e1602060.

(16) Lee, T. H.; Kim, K.; Kim, G.; Park, H. J.; Scullion, D.; Shaw, L.; Kim, M.-G.; Gu, X.; Bae, W.-G.; Santos, E. J. G.; Lee, Z.; Shin, H. S.; Nishi, Y.; Bao, Z. Chemical Vapor-Deposited Hexagonal Boron Nitride as a Scalable Template for High-Performance Organic Field-Effect Transistors. *Chem. Mater.* **2017**, *29*, 2341–2347.

(17) Lyalin, A.; Nakayama, A.; Uosaki, K.; Taketsugu, T. Adsorption and Catalytic Activation of the Molecular Oxygen on the Metal Supported h-BN. *Top. Catal.* **2014**, *57*, 1032–1041.

(18) Uosaki, K.; Elumalai, G.; Noguchi, H.; Masuda, T.; Lyalin, A.; Nakayama, A.; Taketsugu, T. Boron Nitride Nanosheet on Gold as an Electrocatalyst for Oxygen

Reduction Reaction: Theoretical Suggestion and Experimental Proof. *J. Am. Chem. Soc.* **2014**, *136*, 6542–6545.

(19) Lin, S.; Huang, J.; Gao, X. A Cu(111) Supported h-BN Nanosheet: A Potential Low-Cost and High-Performance Catalyst for CO Oxidation. *Phys. Chem. Chem. Phys.* **2015**, *17*, 22097–22105.

(20) Mahvash, F.; Eissa, S.; Bordjiba, T.; Tavares, A. C.; Szkopek, T.; Siaj, M. Corrosion Resistance of Monolayer Hexagonal Boron Nitride on Copper. *Sci. Rep.* **2017**, *7*, 42139.

(21) Corso, M.; Auwärter, W.; Muntwiler, M.; Tamai, A.; Greber, T.; Osterwalder, J. Boron Nitride Nanomesh. *Science* **2004**, *303*, 217–220.

(22) Preobrajenski, A. B.; Vinogradov, A. S.; Ng, M. L.; Ćavar, E.; Westerström, R.; Mikkelsen, A.; Lundgren, E.; Mårtensson, N. Influence of Chemical Interaction at the Lattice-Mismatched h-BN/Rh(111) and h-BN/Pt(111) Interfaces on the Overlayer Morphology. *Phys. Rev. B* **2007**, *75*, 245412.

(23) Joshi, S.; Ecija, D.; Koitz, R.; Iannuzzi, M.; Seitsonen, A. P.; Hutter, J.; Sachdev, H.; Vijayaraghavan, S.; Bischoff, F.; Seufert, K.; Barth, J. V.; Auwärter, W. Boron Nitride on Cu(111): an Electronically Corrugated Monolayer. *Nano Lett.* **2012**, *12*, 5821–5828.

(24) Zum Farwick Hagen, F. H.; Zimmermann, D. M.; Silva, C. C.; Schlueter, C.; Atodiresei, N.; Jolie, W.; Martinez-Galera, A. J.; Dombrowski, D.; Schroder, U. A.; Will, M.; Lazic, P.; Caciuc, V.; Blugel, S.; Lee, T.-L.; Michely, T.; Busse, C. Structure and Growth of Hexagonal Boron Nitride on Ir(111). *ACS Nano* **2016**, *10*, 11012–11026.

(25) Garnica, M.; Schwarz, M.; Ducke, J.; He, Y.; Bischoff, F.; Barth, J. V.; Auwärter, W.; Stradi, D. Comparative Study of the Interfaces of Graphene and Hexagonal Boron Nitride with Silver. *Phys. Rev. B* **2016**, *94*, 155431.

(26) Schulz, F.; Drost, R.; Hämäläinen, S. K.; Demonchaux, T.; Seitsonen, A. P.; Liljeroth, P. Epitaxial Hexagonal Boron Nitride on Ir(111): A Work Function Template. *Phys. Rev. B* **2014**, *89,* DOI: 10.1103/PhysRevB.89.235429.

(27) Auwärter, W.; Kreutz, T. J.; Greber, T.; Osterwalder, J. XPD and STM Investigation of Hexagonal Boron Nitride on Ni(111). *Surf. Sci.* **1999**, *429*, 229–236.

(28) Muntwiler, M.; Zhang, J.; Stania, R.; Matsui, F.; Oberta, P.; Flechsig, U.; Patthey, L.; Quitmann, C.; Glatzel, T.; Widmer, R.; Meyer, E.; Jung, T. A.; Aebi, P.; Fasel, R.; Greber, T. Surface Science at the PEARL Beamline of the Swiss Light Source. *J. Synchrotron Rad.* **2017**, *24*, 354–366.

(29) Mahvash, F.; Paradis, E.; Drouin, D.; Szkopek, T.; Siaj, M. Space-Charge Limited Transport in Large-Area Monolayer Hexagonal Boron Nitride. *Nano Lett.* **2015**, *15*, 2263–2268.

(30) Feigelson, B. N.; Bermudez, V. M.; Hite, J. K.; Robinson, Z. R.; Wheeler, V. D.; Sridhara, K.; Hernandez, S. C. Growth and Spectroscopic Characterization of Monolayer and Few-Layer Hexagonal Boron Nitride on Metal Substrates. *Nanoscale* **2015**, *7*, 3694–3702.

(31) Gómez Díaz, J.; Ding, Y.; Koitz, R.; Seitsonen, A. P.; Iannuzzi, M.; Hutter, J. Hexagonal Boron Nitride on Transition Metal Surfaces. *Theor. Chem. Acc.* **2013**, *132*, 217.

(32) Koitz, R.; Seitsonen, A. P.; Iannuzzi, M.; Hutter, J. Structural and Electronic Properties of a Large-Scale Moire Pattern of Hexagonal Boron Nitride on Cu(111) Studied with Density Functional Theory. *Nanoscale* **2013**, *5*, 5589–5595.

(33) Laskowski, R.; Blaha, P.; Schwarz, K. Bonding of Hexagonal BN to Transition Metal Surfaces: An ab initio Density-functional Theory Study. *Phys. Rev. B* **2008**, *78*, 45409.

(34) Siegel, G.; Ciobanu, C. V.; Narayanan, B.; Snure, M.; Badescu, S. C. Heterogeneous Pyrolysis: A Route for Epitaxial Growth of hBN Atomic Layers on Copper Using Separate Boron and Nitrogen Precursors. *Nano Lett.* **2017**, *17*, 2404–2413.

(35) Moritz, W.; Wang, B.; Bocquet, M.-L.; Brugger, T.; Greber, T.; Wintterlin, J.; Günther, S. Structure Determination of the Coincidence Phase of Graphene on Ru(0001). *Phys. Rev. Lett.* **2010**, *104*, 136102.

(36) Martoccia, D.; Björck, M.; Schlepütz, C. M.; Brugger, T.; Pauli, S. A.; Patterson, B. D.; Greber, T.; Willmott, P. R. Graphene on Ru(0001): A Corrugated and Chiral Structure. *New J. Phys.* **2010**, *12*, 43028.

(37) Roth, S.; Matsui, F.; Greber, T.; Osterwalder, J. Chemical Vapor Deposition and Characterization of Aligned and Incommensurate Graphene/Hexagonal Boron Nitride Heterostack on Cu(111). *Nano Lett.* **2013**, *13*, 2668–2675.

(38) Li, Q.; Zou, X.; Liu, M.; Sun, J.; Gao, Y.; Qi, Y.; Zhou, X.; Yakobson, B. I.; Zhang, Y.; Liu, Z. Grain Boundary Structures and Electronic Properties of Hexagonal Boron Nitride on Cu(111). *Nano Lett.* **2015**, *15*, 5804–5810.

(39) Uchida, Y.; Iwaizako, T.; Mizuno, S.; Tsuji, M.; Ago, H. Epitaxial Chemical Vapour Deposition Growth of Monolayer Hexagonal Boron Nitride on a Cu(111)/Sapphire Substrate. *Phys. Chem. Chem. Phys.* **2017**, *19*, 8230–8235.

(40) Müller, F.; Hüfner, S.; Sachdev, H.; Laskowski, R.; Blaha, P.; Schwarz, K. Epitaxial Growth of Hexagonal Boron Nitride on Ag(111). *Phys. Rev. B* **2010**, *82*, 113406.

(41) Straumanis, M. E.; Yu, L. S. Lattice Parameters, Densities, Expansion Coefficients and Perfection of Structure of Cu and of Cu–In α Phase. *Acta Cryst. A* **1969**, *25*, 676–682.

(42) Artaud, A.; Magaud, L.; Le Quang, T.; Guisset, V.; David, P.; Chapelier, C.; Coraux, J. Universal Classification of Twisted, Strained and Sheared Graphene Moire Superlattices. *Sci. Rep.* **2016**, *6*, 25670.

(43) Zeller, P.; Günther, S. What are the Possible Moiré Patterns of Graphene on Hexagonally Packed Surfaces?: Universal Solution for Hexagonal Coincidence Lattices, Derived by a Geometric Construction. *New J. Phys.* **2014**, *16*, 83028.

(44) Giannozzi, P.; Baroni, S.; Bonini, N.; Calandra, M.; Car, R.; Cavazzoni, C.; Ceresoli, D.; Chiarotti, G. L.; Cococcioni, M.; Dabo, I.; Dal Corso, A.; Gironcoli, S. de; Fabris, S.; Fratesi, G.; Gebauer, R.; Gerstmann, U.; Gougoussis, C.; Kokalj, A.; Lazzeri, M.; Martin-Samos, L. *et al.* QUANTUM ESPRESSO: A Modular and Open-Source Software Project for Quantum Simulations of Materials. *J. Phys. Cond. Matter* **2009**, *21*, 395502.

(45) Lee, K.; Murray, É. D.; Kong, L.; Lundqvist, B. I.; Langreth, D. C. Higher-Accuracy van der Waals Density Functional. *Phys. Rev. B* **2010**, *82*, 81101.

(46) Hamada, I. van der Waals Density Functional Made Accurate. *Phys. Rev. B* **2014**, *89*, 121103.

(47) Klimeš, J.; Bowler, D. R.; Michaelides, A. Van der Waals Density Functionals Applied to Solids. *Phys. Rev. B* **2011**, *83*, 195131.

(48) Mohn, F.; Gross, L.; Meyer, G. Measuring the Short-Range Force Field Above a Single Molecule with Atomic Resolution. *Appl. Phys. Lett.* **2011**, *99*, 53106.

(49) Schuler, B.; Liu, W.; Tkatchenko, A.; Moll, N.; Meyer, G.; Mistry, A.; Fox, D.; Gross, L. Adsorption Geometry Determination of Single Molecules by Atomic Force Microscopy. *Phys. Rev. Lett.* **2013**, *111*, 106103.

(50) Patera, L. L.; Liu, X.; Mosso, N.; Decurtins, S.; Liu, S.-X.; Repp, J. Crystallization of a Two-Dimensional Hydrogen-Bonded Molecular Assembly:

Evolution of the Local Structure Resolved by Atomic Force Microscopy. *Angew. Chem., Int. Ed. Engl.* **2017,** DOI: 10.1002/anie.201705338.

(51) Onoda, J.; Ondracek, M.; Jelinek, P.; Sugimoto, Y. Electronegativity Determination of Individual Surface Atoms by Atomic Force Microscopy. *Nat. Commun.* **2017**, *8*, 15155.

(52) van der Heijden, N. J.; Hapala, P.; Rombouts, J. A.; van der Lit, J.; Smith, D.; Mutombo, P.; Svec, M.; Jelinek, P.; Swart, I. Characteristic Contrast in Δf_{min} Maps of Organic Molecules Using Atomic Force Microscopy. *ACS Nano* **2016**, *10*, 8517–8525.

(53) Weymouth, A. J.; Wutscher, T.; Welker, J.; Hofmann, T.; Giessibl, F. J. Phantom Force Induced by Tunneling Current: A Characterization on Si(111). *Phys. Rev. Lett.* **2011**, *106*, 226801.

(54) Preobrajenski, A. B.; Vinogradov, A. S.; Mårtensson, N. Monolayer of h-BN Chemisorbed on Cu(111) and Ni(111): The Role of the Transition Metal 3d States. *Surf. Sci.* **2005**, *582*, 21–30.

(55) Preobrajenski, A. B.; Nesterov, M. A.; Ng, M. L.; Vinogradov, A. S.; Mårtensson, N. Monolayer h-BN on Lattice-Mismatched Metal Surfaces: On the Formation of the Nanomesh. *Chem. Phys. Lett.* **2007**, *446*, 119–123.

(56) Orlando, F.; Lacovig, P.; Omiciuolo, L.; Apostol, N. G.; Larciprete, R.; Baraldi, A.; Lizzit, S. Epitaxial Growth of a Single-Domain Hexagonal Boron Nitride Monolayer. *ACS Nano* **2014**, *8*, 12063–12070.

(57) Koepke, J. C.; Wood, J. D.; Chen, Y.; Schmucker, S. W.; Liu, X.; Chang, N. N.; Nienhaus, L.; Do, J. W.; Carrion, E. A.; Hewaparakrama, J.; Rangarajan, A.; Datye, I.; Mehta, R.; Haasch, R. T.; Gruebele, M.; Girolami, G. S.; Pop, E.; Lyding, J. W. Role of Pressure in the Growth of Hexagonal Boron Nitride Thin Films from Ammonia-Borane. *Chem. Mater.* **2016**, *28*, 4169–4179.

(58) Woodruff, D. P. Normal Incidence X-Ray Standing Wave Determination of Adsorbate Structures. *Prog. Surf. Sci.* **1998**, *57*, 1–60.

(59) Batterman, B. W.; Cole, H. Dynamical Diffraction of X Rays by Perfect Crystals. *Rev. Mod. Phys.* **1964**, *36*, 681–717.

(60) Patel, J. R.; Berreman, D. W.; Sette, F.; Citrin, P. H.; Rowe, J. E.; Cowan, P. L.; Jach, T.; Karlin, B. Substrate Surface Relaxation for Cl and S on Cu(001). *Phys. Rev. B* **1989**, *40*, 1330–1333.

(61) Usachov, D.; Adamchuk, V. K.; Haberer, D.; Grüneis, A.; Sachdev, H.; Preobrajenski, A. B.; Laubschat, C.; Vyalikh, D. V. Quasifreestanding Single-Layer Hexagonal Boron Nitride as a Substrate for Graphene Synthesis. *Phys. Rev. B* **2010**, *82,* DOI: 10.1103/PhysRevB.82.075415.

(62) Neek-Amal, M.; Beheshtian, J.; Sadeghi, A.; Michel, K. H.; Peeters, F. M. Boron Nitride Monolayer: A Strain-Tunable Nanosensor. *J. Phys. Chem. C* **2013**, *117*, 13261–13267.

(63) Berkó, A.; Solymosi, F. Adsorption of Nitrogen Atoms on Cu(111), Rh(111) and Pt(110) Surfaces. *Appl. Surf. Sci.* **1992**, *55*, 193–202.

(64) Gao, X.; Wang, S.; Lin, S. Defective Hexagonal Boron Nitride Nanosheet on Ni(111) and Cu(111): Stability, Electronic Structures, and Potential Applications. *ACS Appl. Mater. Interfaces* **2016**, *8*, 24238–24247.

(65) Voloshina, E. N.; Fertitta, E.; Garhofer, A.; Mittendorfer, F.; Fonin, M.; Thissen, A.; Dedkov, Y. S. Electronic Structure and Imaging Contrast of Graphene Moire on Metals. *Sci. Rep.* **2013**, *3*, 1072.

(66) La Torre, B. de; Ellner, M.; Pou, P.; Nicoara, N.; Perez, R.; Gomez-Rodriguez, J. M. Atomic-Scale Variations of the Mechanical Response of 2D Materials Detected by Noncontact Atomic Force Microscopy. *Phys. Rev. Lett.* **2016**, *116*, 245502.

(67) Herden, T.; Ternes, M.; Kern, K. Lateral and Vertical Stiffness of the Epitaxial h-BN Monolayer on Rh(111). *Nano Lett.* **2014**, *14*, 3623–3627.

(68) Oyabu, N.; Pou, P.; Sugimoto, Y.; Jelinek, P.; Abe, M.; Morita, S.; Perez, R.; Custance, O. Single Atomic Contact Adhesion and Dissipation in Dynamic Force Microscopy. *Phys. Rev. Lett.* **2006**, *96*, 106101.

(69) Kantorovich, L. N.; Trevethan, T. General Theory of Microscopic Dynamical Response in Surface Probe Microscopy: From Imaging to Dissipation. *Phys. Rev. Lett.* **2004**, *93*, 236102.

(70) Trevethan, T.; Kantorovich, L.; Polesel-Maris, J.; Gauthier, S. Is Atomic-Scale Dissipation in NC-AFM Real?: Investigation Using Virtual Atomic Force Microscopy. *Nanotechnology* **2007**, *18*, 84017.

(71) Pishkenari, H. N. Atomic Interactions Between Metallic Tips and Surfaces in NC-AFM. *J. Phys. D: Appl. Phys.* **2015**, *48*, 125301.

(72) Pease, R. S. An X-Ray Study of Boron Nitride. *Acta Cryst.* **1952**, *5*, 356–361.

(73) Flinn, P. A.; McManus, G. M.; Rayne, J. A. Effective X-Ray and Calorimetric Debye Temperature for Copper. *Phys. Rev.* **1961**, *123*, 809–812.

(74) Sachs, B.; Wehling, T. O.; Katsnelson, M. I.; Lichtenstein, A. I. Adhesion and Electronic Structure of Graphene on Hexagonal Boron Nitride Substrates. *Phys. Rev. B* **2011**, *84,* DOI: 10.1103/PhysRevB.84.195414.

(75) Dean, C. R.; Young, A. F.; Meric, I.; Lee, C.; Wang, L.; Sorgenfrei, S.; Watanabe, K.; Taniguchi, T.; Kim, P.; Shepard, K. L.; Hone, J. Boron Nitride Substrates for High-Quality Graphene Electronics. *Nat. Nanotechnol.* **2010**, *5*, 722–726.

(76) Lin, X.; Xu, Y.; Hakro, A. A.; Hasan, T.; Hao, R.; Zhang, B.; Chen, H. Ab initio optical study of graphene on hexagonal boron nitride and fluorographene substrates. *J. Mater. Chem. C* **2013**, *1*, 1618.

(77) Marom, N.; Bernstein, J.; Garel, J.; Tkatchenko, A.; Joselevich, E.; Kronik, L.; Hod, O. Stacking and registry effects in layered materials: The case of hexagonal boron nitride. *Phys. Rev. Lett.* **2010**, *105*, 46801.

(78) Giessibl, F. J. High-Speed Force Sensor for Force Microscopy and Profilometry Utilizing a Quartz Tuning Fork. *Appl. Phys. Lett.* **1998**, *73*, 3956–3958.

(79) Hesse, R.; Streubel, P.; Szargan, R. Product or Sum: Comparative Tests of Voigt, and Product or Sum of Gaussian and Lorentzian Functions in the Fitting of Synthetic Voigt-Based X-Ray Photoelectron Spectra. *Surf. Interface Anal.* **2007**, *39*, 381–391.

(80) Nicolas, C.; Miron, C. Lifetime Broadening of Core-Excited and -Ionized States. *J. Electron Spectrosc. Relat. Phenom.* **2012**, *185*, 267–272.

(81) Fisher, C. J.; Ithin, R.; Jones, R. G.; Jackson, G. J.; Woodruff, D. P.; Cowie, B. C. C. Non-Dipole Photoemission Effects in X-Ray Standing Wavefield Determination of Surface Structure. *J. Phys. Cond. Matter* **1998**, *10*, L623-L629.

(82) Woodruff, D. P. Surface Structure Determination Using X-Ray Standing Waves. *Rep. Prog. Phys.* **2005**, *68*, 743–798.